Rare Metal Materials and Engineering
Volume 53, Issue 3, March 2024
Available online at www.rmme.ac.cn

Science Press

Cite this article as: Liu Pengyu, Li Hui, Zhang Ruihua, et al. Wear Resistance of Laser Cladding TiC Particle-Reinforced Fe-based Gradient Coating[J]. Rare Metal Materials and Engineering, 2024, 53(03): 632-642. DOI: 10.12442/j.issn.1002-185X.20230190.

ARTICLE

Wear Resistance of Laser Cladding TiC Particle-Reinforced Fe-based Gradient Coating

Liu Pengyu[1], Li Hui[1,3], Zhang Ruihua[1,2], Xiao Mengzhi[1], Wei Xiaohong[2], Yin Yan[2,4], Qu Yuebo[1], Lu Chao[2,5]

[1] Central Iron and Steel Research Institute, Beijing 100081, China; [2] Hardware Knife Cut Industrial Technology Research Institute Yangjiang, Yangjiang 529533, China; [3] Sichuan Provincial Key Lab of Process Equipment and Control, Sichuan University of Science & Engineering, Zigong 643000, China; [4] School of Materials Science and Engineering, Lanzhou University of Technology, Lanzhou 730050, China; [5] School of Materials Science and Engineering, Guangdong Ocean University, Yangjiang 529500, China

Abstract: A high-hardness, wear-resistant gradient ceramic coating was prepared by laser cladding TiC particle-reinforced iron-based powder onto a 40Cr steel substrate to achieve the coating's gradient effect. Scanning electron microscope (SEM), energy dispersive spectroscope (EDS), X-ray diffractometer (XRD), micro-hardness tester, and friction and wear tester were used to investigate the microstructure, phase, hardness, and wear resistance of the cladding layer. Results show that the phase of the cladding layer is mostly austenite, some TiC strengthening phase, and a trace amount of ferrite phase. The cermet coating made of laser cladding TiC particle-reinforced powder has a compact microstructure, and the coating phase composition is essentially the same as the powder composition. The TiC phase, which is responsible for the strengthening effect, is dispersed across the molten pool following a gradient from the bottom to the top. The TiC phase reinforcing the molten pool is partly dissolved, and thus the size of the pool shrinks. Under the laser's intense heat, some TiC strengthening phases develop into shapes like squares, snowflakes, and fish bones. At the base of the molten pool, the TiC phase may develop in three ways, while the TiC strengthening phase is less widely dispersed. The TiC strengthening phase in the center of the molten pool is progressively expanded, and enriched and bridged in the top portion of the molten pool. The cladding layer has a Vickers hardness HV up to 19 602.94 MPa, and under the same circumstances, the friction and wear depth of the coating is only one-fifth of that of the substrate. This results in a considerable improvement in the wear resistance of the substrate.

Key words: laser cladding; TiC; metal ceramic; organizational performance

Medium carbon low alloy structural steel 40Cr is now widely used in connecting rods, shafts, bolts, gears and other components, especially in its quenched and tempered state in which higher strength, plasticity and toughness can be obtained[1]. Degradation of tribological property and corrosion resistance and low hardness are the surface-related phenomena that result in failure of 40Cr steel (similar to AISI 5140) working under aggressive service conditions[2]. In order to improve the friction and wear properties of components, surface strengthening is needed[3–6]. Laser cladding is an effective technique and has been widely used for high-quality coating preparation because of following advantages. Firstly, laser cladding can solve the problem that coatings are too thin and susceptible to cracking compared with those prepared by vapor deposition and plasma spraying. Secondly, the laser cladding coating has stronger bond performance than the coatings prepared by other methods[3–9].

TiC has a crystal structure that is known as face-centered cubic (fcc) one, and its lattice constant is equal to 0.4328 nm[10–12]. The atomic configuration constitutes of Ti atoms are located at six corners as well as the surface centers, and C atoms may be found in the cube's center and the middle of

Received date: April 07, 2023
Foundation item: National Natural Science Foundation of China (52161007); Key Technical Project of Shenzhen Innovation and Entrepreneurship Plan (JSGG20210420091802007); Guangdong Province Science and Technology Special Fund Project (SDZX2020009); Sichuan Provincial Key Lab of Process Equipment and Control Open Fund Project (GK202104, GK202106)
Corresponding author: Zhang Ruihua, Ph. D., Research Fellow, Central Iron and Steel Research Institute, Beijing 100081, P. R. China, Tel: 0086-662-3837260, E-mail: 391079595@qq.com

Copyright © 2024, Northwest Institute for Nonferrous Metal Research. Published by Science Press. All rights reserved.

each edge. Eight C atoms octahedrally coordinate one Ti atom, while each C atom is coordinated octahedrally by eight Ti atoms. Because of this, each titanium atom is bound to six carbon atoms, and each carbon atom is bonded to six titanium atoms. The Ti-C bonds are both strong and covalent[13–14]. It is widely used in the chemical industry, machinery, electronics, aerospace, and biomedical engineering due to several characteristics, including its high level of hardness, high melting point, high elastic modulus, low density, easy access to resources, and cheap cost[13-17].

In recent years, more and more studies have focused on the preparation of TiC-reinforced composite coatings by laser cladding in-situ growth or addition of strengthening phases[18]. Yang et al[19] prepared TiC particle-reinforced nickel-based composite coating using titanium powder, graphite and nickel-based alloy, and applied it to 45# steel by laser cladding technology. The coating shows good metallurgical bonding force, TiC phase is continuously and evenly distributed, and there are no pores and cracks in the coating. Xu et al[20] used Inconel 625 wire with TiC particle as reinforcing phase to form a nickel-based coating with high hardness and good mechanical properties on the surface of 316L stainless steel. Fabrication of a TiC-reinforced nickel-metal composite coating was accomplished by Liu et al[21] using an in-situ metallurgical method on a Ti-6Al-4V substrate. TiC/Ti gradient composites with TiC content from 0vol% to 40vol% were developed by Zhang et al[22] using laser melting deposition. Gu et al[23] found that the interface bonding ability between the larger unmelted ceramic particles and the matrix is poor, and during the tensile process, the contact between the ceramic particles and the matrix is fragile and easy to be destroyed, which may lead to premature cracking of titanium matrix composites. Qi et al[24] successfully cladded a cobalt-based alloy on the surface of 42CrMo substrate by alternating magnetic field under the condition of magnetic field oscillation. As a direct consequence of the provided magnetic field, the microstructure of the cladding layer is dramatically enhanced, and the layer's hardness is significantly increased. TiC-TiB_2/Al-12Si aluminum matrix composites were in-situ prepared by ultrasonic-assisted laser deposition technology by Zhao et al[25], which improved the wear resistance of the samples.

To improve the tribological property and to broaden 40Cr steel application scenarios, we developed a laser cladding method which is suitable for single-pass laser cladding to prepare TiC particle-reinforced Fe-based coatings on 40Cr steel substrate with controllable TiC content, controllable gradient, low cost, and stable performance, which is of great theoretical significance and application value to further improve friction and wear properties of 40Cr steel and to promote the application of TiC-reinforced metal matrix composite coating.

1 Experiment

The substrate was made of a 40Cr steel plate with 6 mm in thickness and 60 mm in length. The TiC particle-reinforced powder was prepared by the Beijing General Research Institute of Mining &Metallurgy. Table 1 and Fig.1 display the powder's composition and morphology, respectively.

The integrated cladding technology from Hardware Knife Cut Industrial Technology Research Institute Yangjiang was used to prepare the coating. The powder feeder was ABB robot of model PD150, the laser was IPG YLS-2000, the laser cladding nozzle was Shanghai Gaize COX-1, and the mobile control mechanism was an ABB robot of type IRB-2600. 99.99% pure argon was used in the test to move and safeguard the powder. The particular procedure is described in Table 2.

The automated X-ray diffractometer (XRD) was used for phase analysis. The tube voltage was set at 40 kV, the tube current was set at 200 mA, and the scanning speed was set at 5°/min. After the TiC particle-reinforced powder alloy samples were cut into blocks of 10 mm^2 using a wire-cutting machine, the powder and the blocks were immersed in epoxy resin to be ground and polished. The microstructure of the structure was exposed by aqua regia erosion solution. Carl Zeiss SEM EVO 18 was used to investigate the powder's microstructure, cladding layer, and friction and wear surface. Oxford EDS was used to analyze the composition.

To determine the Vickers hardness of the coating's cross-section, a German KB30S tester was used. During the experiment, we employed a loading of 2.94 N and a loading duration of 15 s. In order to get an accurate value of hardness, measurements were taken every 0.2 mm along the substrate. Five sets of parallel indentations were made simultaneously at each place for defect identification.

The coatings were put through their paces with reciprocating dry sliding friction and wear tests using a Bruker UMT Tribolab tester at room temperature and atmospheric pressure. As one component of the friction pair, WC grinding ball with 8 mm in diameter and a hardness of 94 HRA was used. An applied load of 50 N was maintained for 40 min at a frequency of 2 Hz with an amplitude of 5 mm, while the sliding speed was 20 mm/s. In order to investigate the wear

Table 1 Chemical composition of TiC particle-reinforced powder (wt%)

TiC	Ni	Mo	Mn	Fe	Other elements
80	1	0.45	3.2	15.15	≤0.2

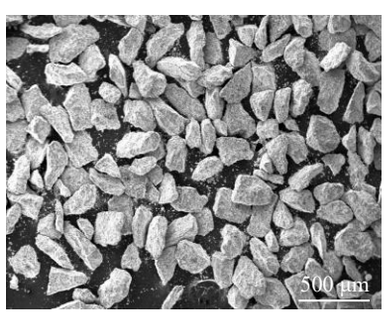

Fig.1 SEM image of TiC particle-reinforced powder

morphology of the coating and the substrate, a Bruker Contour GT white light interference 3D optical profilometer was used.

2 Results and Discussion

2.1 Microstructure and phase composition analysis of TiC particle-reinforced powder

Fig.2 reveals the XRD pattern of the TiC particle-reinforced powder. It is clear that the TiC particle-reinforced powder comprises three phases, i. e., TiC, austenite, and trace ferrite phases. According to the investigations, some austenites transform into ferrite during the manufacturing of particle-reinforced powder because of the powder's sluggish cooling rate. The explanation of the metallurgical process of the austenite-ferrite formation mode is: L+TiC→L+TiC+γ→ L+TiC+δ+γ→TiC+γ+δ. This is consistent with Lu's[26] study on the precipitation of ferrite from austenite.

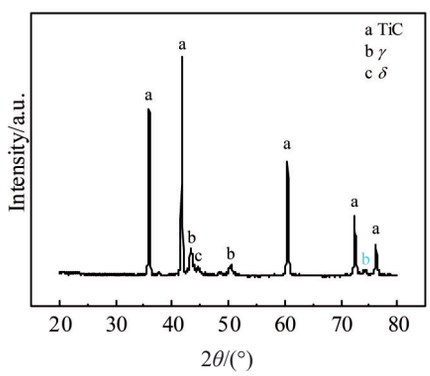

Fig.2 XRD pattern of TiC particle-reinforced powder

Fig. 3 shows the macroscopic morphologies and surface scanning characterization of the powder. According to the SEM image (Fig. 3a), the powder shape shows irregular polygon distribution. Many uniformly distributed ceramic particles inside the powder are shown in Fig.3b. The distance between ceramic particles (Fig.3b) is 0.5–5 μm. The statistical measurement of powder microscopic image (Fig.3b) by Image Pro shows that the size of ceramic particles is 0.5–10 μm. The mass ratio of the strengthening phase to the alloy phase (M_{TiC}: M_{Alloy}=79.97: 20.03) was obtained by statistical conversion analysis of the SEM image (Fig.3b) by Image Pro, which is consistent with the known powder composition (Table 1). It can be seen from Fig. 3c–3f that TiC particles are uniformly embedded in the alloy, and the alloy formed by iron and manganese elements forms a bonding phase between the ceramic particles.

2.2 Vickers hardness analysis of coatings

The Vickers hardness of the coating is shown in Fig. 4. It is clear that from the substrate to the upper part of the coating, the hardness rises. At the same horizontal position, the hardness of the coating is also different. This phenomenon is due to numerous strengthening and alloy phases in the microstructure and the uneven spacing between strengthening phases. The coating has hardness up to 19 602.94 MPa, and it is possible to achieve a gradient distribution of hardness from the bottom to the top of the cladding layer.

Table 2 Processing parameters of laser cladding TiC particle-reinforced powder

Power/W	Speed/mm·s^{-1}	Gas flow/L·min^{-1}	Powder feeding rate/g·s^{-1}	Defocusing amount/mm	Spot diameter/mm
1700	2.5	12	10	16	3

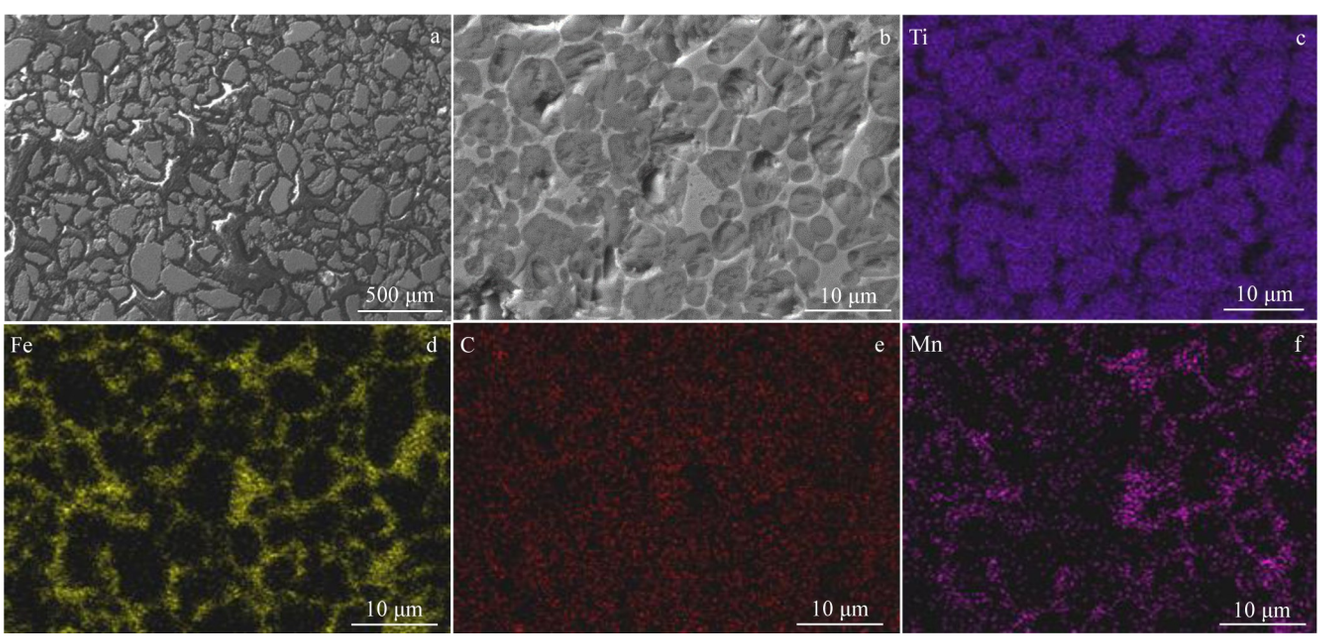

Fig.3 SEM morphologies (a–b) and internal element distributions (c–f) of TiC particle-reinforced powder

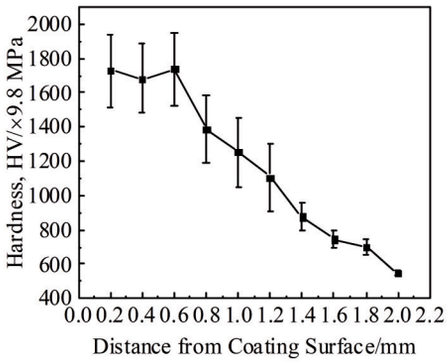

Fig.4 Hardness curve of cladding layer

2.3 Microstructure and phase composition analysis of the coating

Fig.5 shows the XRD patterns of the coating. It shows that the coating mainly comprises three phases: TiC phase, austenite phase and trace ferrite phase. Compared with Fig.2, it is found that the coating phase (Fig. 5) is the same as the powder phase (Fig.2) in constitution. However, the peak of the ferrite phase (Fig.5) is more vital than that of powder (Fig.2). The difference in process of laser cladding and powder preparation may cause this phenomenon. The cooling rate of the cladding process in the molten pool is slower than that of the powder preparation, so the ferrite phase is easier to form in the cladding process.

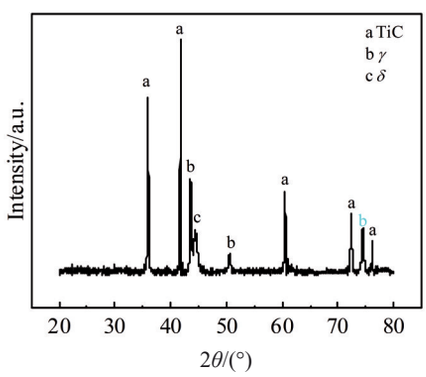

Fig.5 XRD pattern of cladding layer

The particles of the strengthening phase at the bottom of the cladding layer have three different distribution modes. Fig. 6 illustrates the first scenario of the strengthening phase distribution at the base. The scattered TiC particles can be observed in Fig. 6a. Fig. 6b – 6e show the distribution of iron, titanium, carbon and manganese, respectively. The original TiC (Fig. 6a) with a smooth surface and rounded edges is distributed at the bottom, and a small number of particles are agglomerated without noticeable growth trend. The distance between the strengthening phases at the bottom (Fig. 6a) is farther than that between the TiC in the powder (Fig.3). It can be seen in Fig. 6a that the gap between some of the strengthening phases is greater than 10 μm. This indicates that the strengthening phase particles at the bottom migrate along with the flow of the alloy phase in the molten pool during the cladding process. The space between the strengthening phases grows during the movement, and some particles may float upward. The EDS mappings of Fig. 6b – 6e show that the distribution of titanium, iron, and carbon elements corresponds well with the strengthening phase and alloy phase distribution in Fig.6a. By comparing the morphology of TiC in Fig.3b, it can be seen that the morphology of TiC in Fig.6a has no obvious change, which also reflects that the energy received in this region is not enough to allow TiC to grow. The formation mechanism of this region can be explained as follows: in the first step, the laser interacts with the powder; in

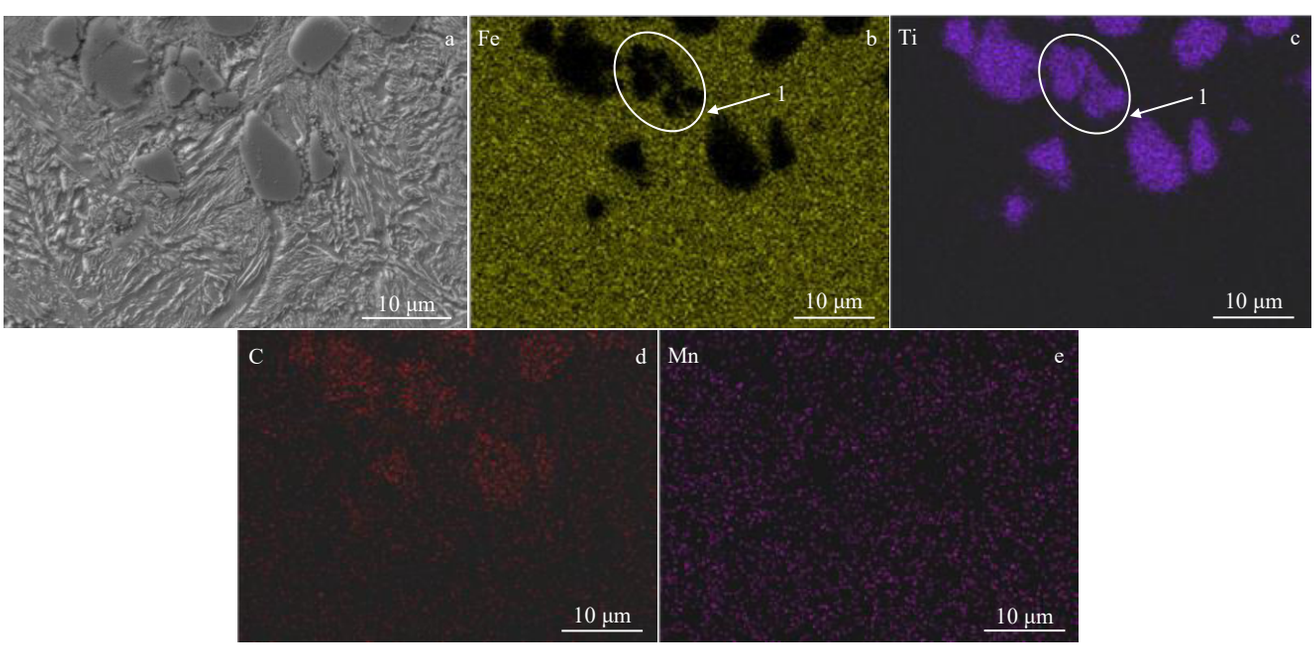

Fig.6 The first distribution of strengthening phase at the bottom of laser cladding coating: (a) SEM morphology and (b–e) EDS mappings

the second step, the powder melts and falls onto the substrate to form a molten pool; in the third step, the continuous powder is transported into the molten pool, which blocks the propagation of the laser to the molten pool. Some areas at the bottom of the molten pool cannot receive the laser energy smoothly, which shortens the interaction time between these areas and the laser or makes these areas not interact with the laser. Moreover, these areas are close to the substrate, the heat disappears quickly, and the temperature decreases rapidly. Therefore, the original TiC particles have yet to melt or obtain Ti and C elements from other regions for growth. This region has completed the solidification process, forming the first morphology. These characteristics are consistent with the results of Lee et al[27].

Fig. 7 shows the second distribution of the bottom strengthening phase. The morphology of TiC can be seen in Fig. 7a. Fig. 7b–7e intuitively show the element mappings of the strengthening phase and the matrix. Many submicron TiC particles are adsorbed around the large TiC particles in Region 1 and 2 (Fig. 7a). These smaller submicron particles grow around the original TiC particles in a "satellite ball" manner. There are many individual TiC submicron particles in Region 3 (Fig. 7a). The size of these individual TiC submicron particles is the same as that in Region 1 and 2, and the distribution of Ti element corresponding to the original TiC particles and submicron TiC particles can be seen in Fig. 7c. The formation mechanism of this region can be explained as follows: firstly, the powder interacts with the laser, and then the powder melts and enters the molten pool to form a melt channel. After the powder interacting with the laser receives more laser energy, the original TiC particles will be affected to complete the metallurgical melting, nucleation, and growth process. In the metallurgical process, TiC particles absorb much energy in the metallurgical process and decompose into Ti and C atoms. Then, Ti and C atoms constantly react to synthesize TiC (Ti+C=TiC). Because the original TiC particles have different sizes, which is affected by laser energy transmission, the shape of TiC particles still shows a diversified distribution in sizes. So, there will be a concentration difference between these TiC particles. In other words, in continuous melting and nucleation of TiC particles with different volumes, a concentration gradient is formed at the boundary of large TiC particles and small TiC particles. The solute at the boundary of small particles will diffuse to the boundary of large particles due to high concentration. In the process of element diffusion, the concentration gradient at the boundary of large TiC particles and small TiC particles becomes larger. Therefore, small particles will continue to dissolve in this area, and large particles will continue to grow. The metallurgical phenomena of melting and solidifying of TiC particles in this study are consistent with the results in Ref. [28–29]. However, compared with the TiC particles in Fig. 6, the TiC particles in Fig. 7 obtain more laser energy. Therefore, the TiC particles in Fig. 7 undergo a complete metallurgical reaction. However, part of the energy transmitted by the laser is blocked by the powder entering the laser, which hinders this region (Fig. 7) from obtaining more energy. Moreover, this region is close to the matrix, and the temperature decreases rapidly. Therefore, the small TiC particles cannot entirely melt and decompose, and the "satellite" particles on the large particles have not grown. This region has completed the solidification process of the molten pool, and then the morphology of the strengtheming phase (Fig.7) appears.

Fig. 8 depicts the third growth mode of TiC particles at the bottom of the coating. The high-resolution SEM image (Fig. 8a) shows the dendritic growth morphology of TiC, and the distribution of manganese, titanium, iron, and carbon

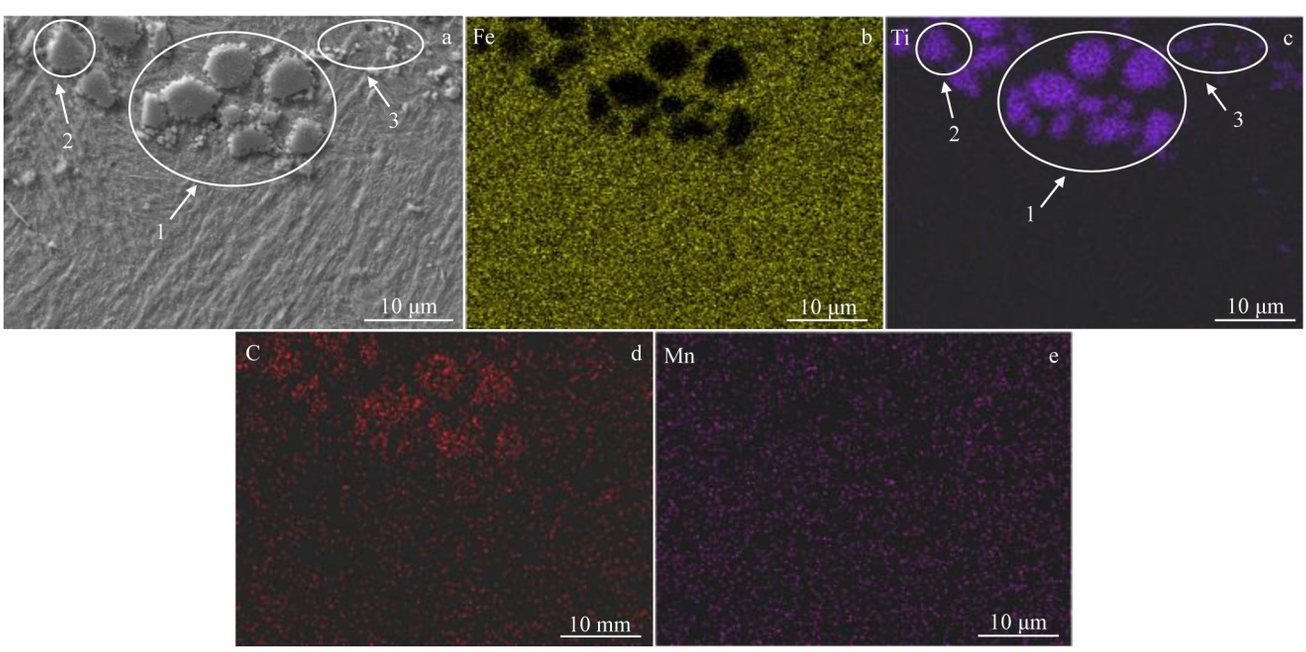

Fig.7 The second distribution of strengthening phase at the bottom of laser cladding coating: (a) SEM morphology and (b–e) EDS mappings

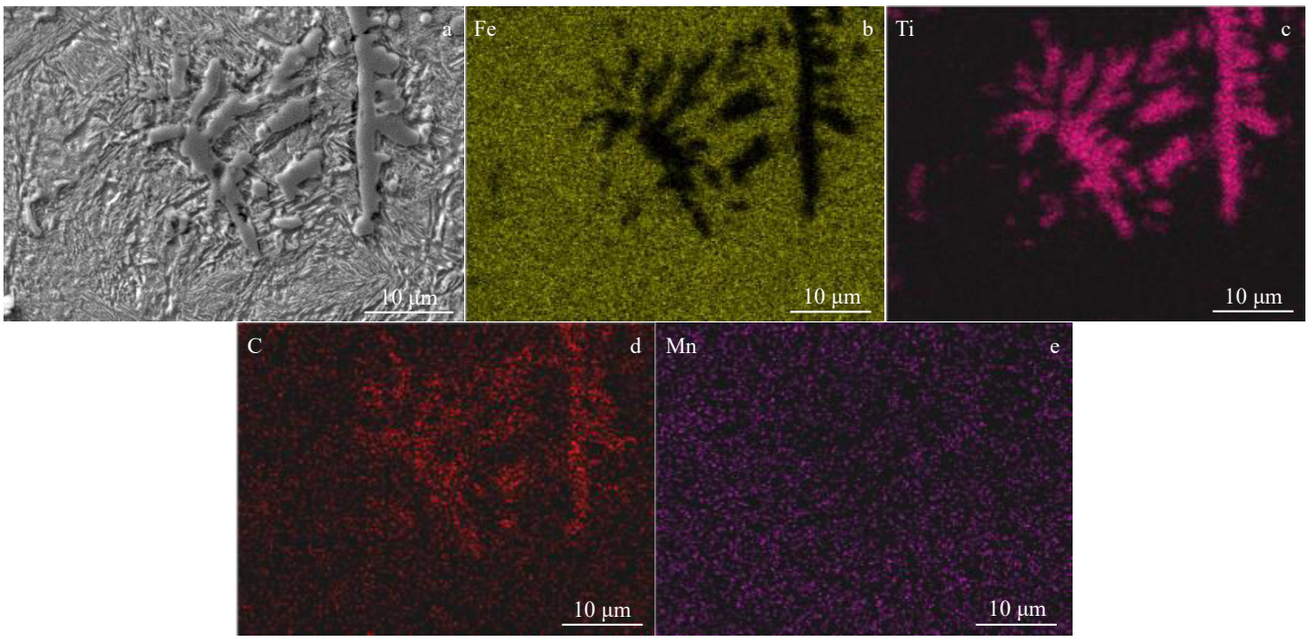

Fig.8 The third distribution of strengthening phase at the bottom of laser cladding coating: (a) SEM morphology and (b–e) EDS mappings

elements in Fig.8b–8e shows a good correspondence with the SEM image (Fig. 8a). Fig. 8a shows a smooth and round boundary without obvious angular dendrites, which proves that the TiC particles in the third phenomenon (Fig. 8) grow more thoroughly than those in the first (Fig.6) and the second (Fig. 7) phenomena. It can be speculated that the powder transported from the powder feeding device may not effectively hinder the laser from entering this region (Fig.8a), and then the TiC particles in this region (Fig.8a) get sufficient energy to grow and to form a dendritic structure. It is also found by He et al[30] that TiC is more prone to dendritic formation when subjected to a laser action, which agrees with this research findings. Nevertheless, it is possible that the growth direction of the secondary dendrite arm of the dendrite is not perpendicular to the primary dendrite due to the influence of the heat dissipation direction in this region.

Fig. 9 depicts the SEM image at the middle and lower part of coating. Compared with the TiC particles at the bottom, the quantity of TiC particles in the middle and lower portions rises, and the size of the particles in the middle and lower parts is larger than that at the bottom. At the same time, from the region in Fig. 8a, it can be seen that the original TiC develops into butterfly-shaped particles, and some square TiC particles appear in the cladding layer. The analysis shows that there is a longer process of strengthening phase decomposition and growth in the middle and lower parts; that is, TiC in the alloy phase decomposes into Ti and C elements during the cladding process, and the thermodynamic driving force of the TiC synthesis reaction is much larger than that of Fe_2Ti, so Ti will be consumed by the Ti + C = TiC reaction. In other words, the cladding process causes TiC to decompose into Ti and C elements. There will be no development of Fe_2Ti; after the consumption of C, there will be no residual C to react with Fe to produce Fe_3C; after quick cooling, Mn, Ni, and other elements will stay in the high-temperature structure, which encourages the creation of austenite[31–32]. In addition, the heat dissipation rate in the middle and lower parts of the molten pool is lower than that at the bottom, and there is a concentration gradient between large and small particles. The original TiC particles with larger particle sizes in this area are easier to grow, forming the structure at Fig.9.

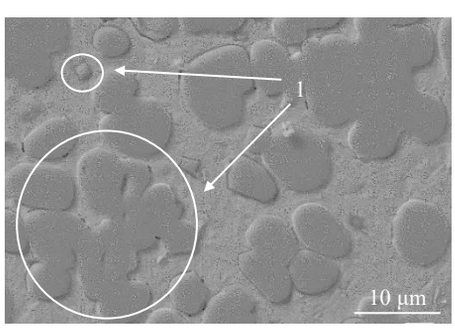

Fig.9 SEM morphology of the middle and lower part of the laser cladding coating

SEM image (Fig. 10a) and EDS mappings (Fig. 10b – 10e) reveal the morphology and element distribution. It can be seen that many round TiC particles are evenly distributed in Fig.10a. The number of TiC particles shown in Fig.6–Fig.9 is less than that shown in Fig.10, and the distance between TiC particles also shows a decreasing trend, indicating that TiC at the bottom may be affected by buoyancy and Marangoni convection and move to the middle. Region 1 (Fig.10a) shows that many small TiC particles gather together and grow into large TiC particles. These tiny particles collide together under the action of buoyancy and Marangoni convection. Because the small TiC particles have a strong adsorption effect, they

agglomerate and grow up, forming the morphology shown in Region 1 (Fig.10a). The boundary of many small TiC particles in Region 1 (Fig. 10a) that has not disappeared well demonstrates the agglomeration growth.

The picture of the top of the coating can be seen in Fig.11, and the element distribution maps can be found in Fig. 11b–11e. Compared with the distribution of strengthening phases in the powder (Fig.5), bottom (Fig.6), and middle (Fig.10), the TiC in the top (Fig. 11) accounts for a more significant proportion, and the distance between particles is more minor. This suggests that the TiC in the bottom and middle floats to the upper part and gathers obviously under the influence of buoyancy and Marangoni convection, and there is a phenomenon of bridging growth between TiC. Fig. 11a – 11c make this point abundantly clear. It can also be observed that TiC exhibits a "genetic growth phenomenon". As shown in Fig.11a, the surface of the reinforced phase has a morphology similar to that of the powder, and it has a somewhat more uneven texture than the surface of the bottom and middle regions does. Therefore, it is thought that the reinforced phase only emerges as bridging growth while keeping some of the morphological traits of the original powder, because of the quick heat dissipation in the higher portion of the molten pool.

The floating mechanism of TiC particles is analyzed. Fig.12a and 12b show the melting and floating mechanisms of TiC particles-reinforced powder by laser cladding, respectively. The laser radiates to the powder, and the powder melts into droplets. In melting process, the strengthening phase particles are mainly affected by three forces: gravity G, buoyancy F_b, and force generated by Marangoni convection F_m. During the falling process of the powder, the powder absorbs the heat transferred by the laser and melts. The lower density of TiC, compared with Fe ($\rho_{TiC}<\rho_{Fe}$), results in $G<F_b$, so TiC inside the powder is partially floated by Marangoni convecton force and buoyancy during the melting process of the powder. When the powder falls on the substrate to form a molten pool, the powder and the substrate absorb more laser energy to melt more fully, and the molten pool has better fluidity than it in the time at which the powder is just heated and melted. At the same time, the Marangoni convection caused by the surface tension further promotes the floating of TiC, so the gradient coating of Fig.12b is formed.

2.4 Analysis of friction and wear properties of the coating

The friction and wear statistics of the substrate are shown in Fig. 13. The friction and wear between the substrate and the coating are shown in Fig. 13a, which includes both the width and depth curves. The three-dimensional reconstruction of the coating's wear and friction morphology is shown in Fig. 13b. The three-dimensional reconstruction of the morphology of the friction and wear on the substrate is shown in Fig. 13c. According to Fig. 13a, the depth of the substrate is about five times larger than that of the coating when looking from the standpoint of friction and wear depth. Based on Fig. 13b–13c, it is easier to see that the coating is fundamentally a plane and the substrate has wear pits. As a result, the laser cladding coating well protects the 40Cr steel from wear and tear and enhances the level of wear resistance the 40Cr steel.

Fig. 14 demonstrates the friction and wear morphology and surface element distributions of 40Cr steel. Both friction and wear require two touched objects to move relatively[26–27]. This is a common knowledge. The material on the contact surface is progressively removed due to the interaction and friction between the objects. The three steps often involved in the wear process are surface contact, damage to the surface layer, and the shedding of debris caused by wear. The friction between the alloy phase and the friction ball is one of the

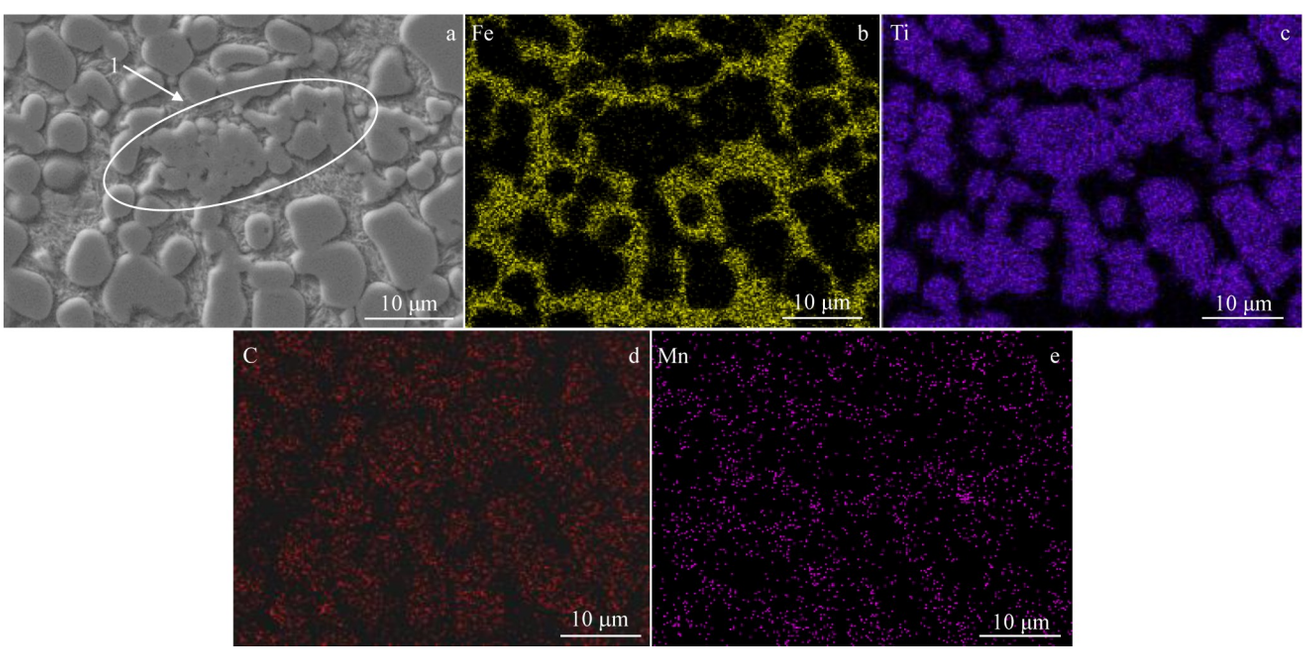

Fig.10 SEM morphology (a) and EDS mappings (b–e) of the middle of laser cladding coating

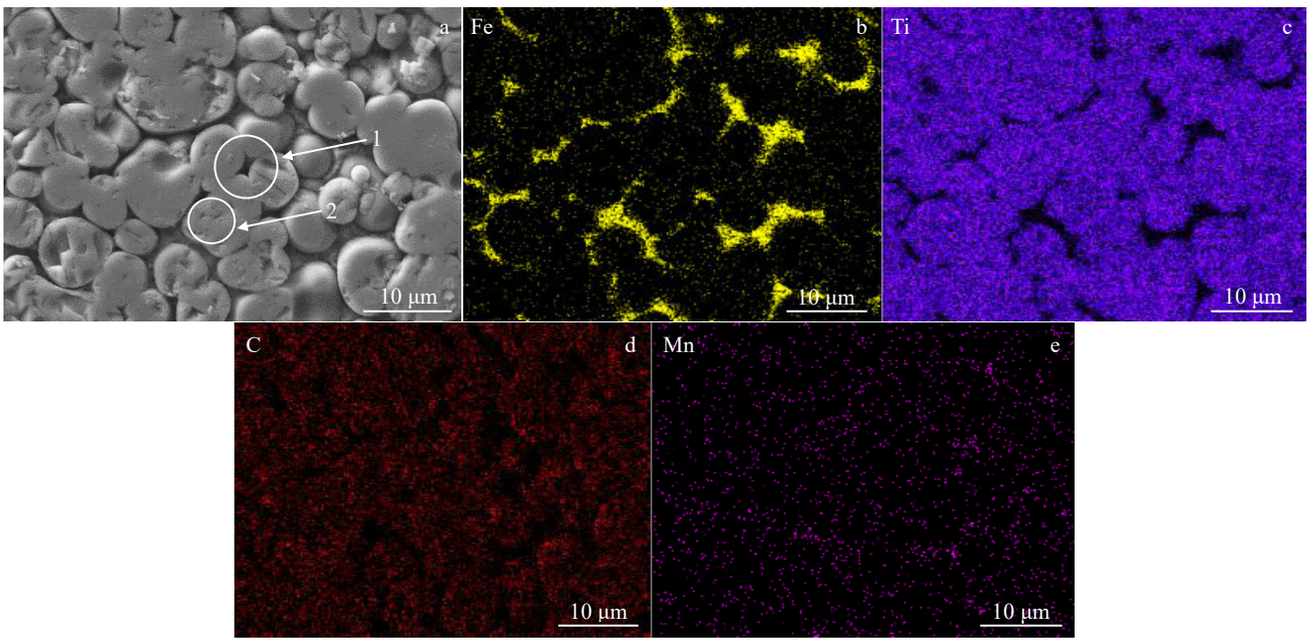

Fig.11 SEM morphology (a) and EDS mappings (b–e) of the upper part of laser cladding coating

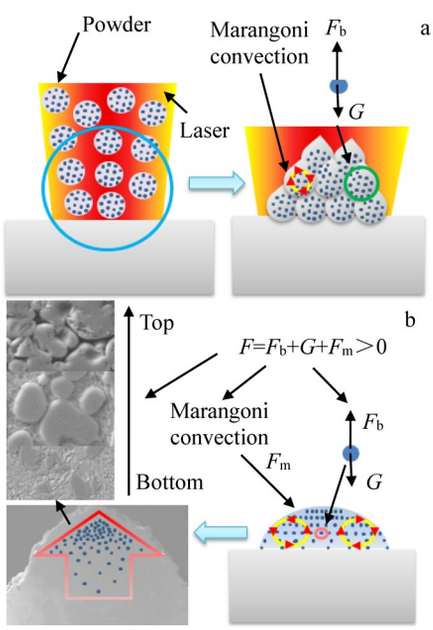

Fig.12 Analysis of melting (a) and floating (b) mechanisms of TiC particles

matrix ' s primary units of friction and wear[33]. The other primary unit is the mutual meshing, collision, and plastic deformation between the surface asperities[34]. The force between the molecules causes the surfaces to stick together when they are close enough. One of the reasons for friction is the energy loss caused during the sliding process, also known as the adhesive effect[35]. When the two surfaces are close enough, the adhesion effect causes the surfaces to adhere together. The asperity peak is exposed to considerable contact stress and plastic deformation due to the action of an applied load, which finally leads to the contact point "cold welding" together[36].

The asperity peak is subjected to significant contact stress because the contact between the surfaces occurs in the tiny space between the asperity peaks. When the two surfaces move relatively, the solder connection is severed, as shown in Area 1 of Fig. 14a, and the hard asperities are implanted into the softer contact surface, which results in furrows on the surface of the softer part, as shown in Fig. 14a. Following the generation of the furrows, there will be debris between the two moving contacting surfaces, which will undergo deformation due to the extrusion movement. Concurrently, as a consequence, the formation of furrows will be altered indirectly. The observable external manifestations include the furrows becoming broader or distorted, as shown in Fig. 14a, and the oxidation process also occurs at the contact region of the two friction surfaces. This is due to the high temperature and pressure during the friction operation. Because there is a significant quantity of oxygen found on the surface, as seen in Fig. 14c, it can be deduced that the worn form of the matrix is composed of both adhesive wear and abrasive wear.

The nature of the material is one of the primary factors that may significantly impact the friction and wear qualities of the material. However, friction can cause surface damage and wear[37]. In the same vein, friction is another mechanism that may change the kinetic energy into thermal energy. Thus, when heat and force are combined, several physical and chemical changes occur on the friction surface. These changes cause friction surface changes, including element distribution, plastic deformation, oxidation, phase transformation, and material transfer[38–39]. The friction and wear surfaces of the coating can be seen in Fig. 15a. There are a few pits on the

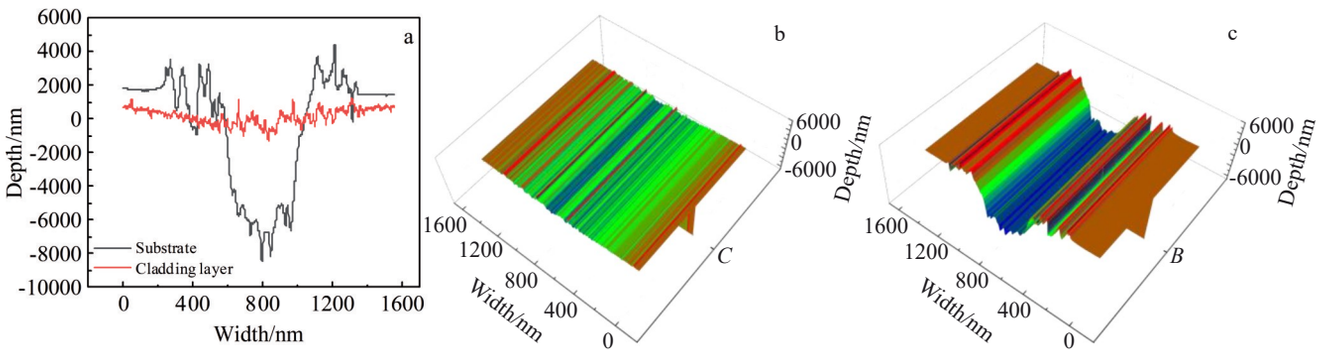

Fig.13 Two-dimensional contour (a) and three-dimensional morphology reconstructions of friction wear of cladding coating (b) and substrate (c)

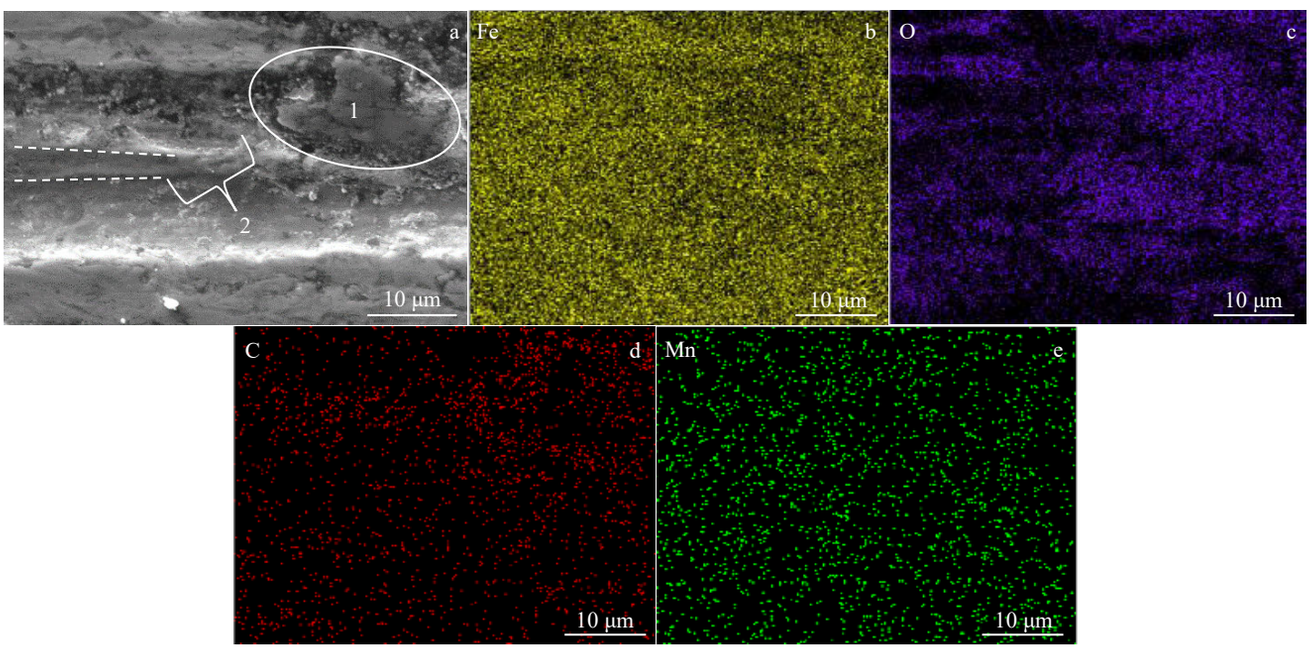

Fig.14 SEM morphology (a) and EDS mappings (b–e) of friction and wear of substrate

surface, as seen in Fig. 15a, but most worn surfaces are relatively smooth and free of any visible furrows. When the friction pairs slide against one another, it is generally agreed that the surface with lower friction coefficient is subjected to the action of a cyclic load. The surface layer produces shear plastic deformation, and accumulation occurs constantly. Due to the consistent buildup of shear deformation, dislocation accumulation occurs gradually in the deformation layer underneath the surface layer, ultimately producing fractures or holes. Since the normal tension parallel to the surface prevents fracture propagation in the depth direction, the hole and crack merge at a certain depth and expand in a nearly parallel direction. This occurs because every stress is parallel to the surface. When the fracture extends to the surface, the surface material will create a thin and protracted wear layer before ultimately falling off in flake wear debris. This happens when the crack has reached the surface. In conjunction with the surface mappings, it is possible to observe that the strengthening phase particles are dispersed throughout the package of the mesh structure. At the same time, the SEM and EDS results are compared. In the SEM image (Fig.15a), a vast smooth region can be observed, which does not consist entirely of TiC ceramic particles. As a result, it is believed that the flake wear debris is peeled off during the friction process, it is welded together with TiC and the binder phase around it, and the wear that can be seen in the picture is caused by the plastic change that occurs as a result of the action of pressure. In addition, as shown in Fig. 15d, the worn surface contains a significant amount of oxygen elements; hence, it is hypothesized that the oxidation process occurs on the surface. Because oxygen is simpler to react with titanium to generate titanium oxide and subsequently reacts with iron to form iron oxide, the wear surface is composed of titanium and iron oxides[40–41]; this can be demonstrated by the Gibbs free energy of oxygen and alloy components such as iron and titanium alloys.

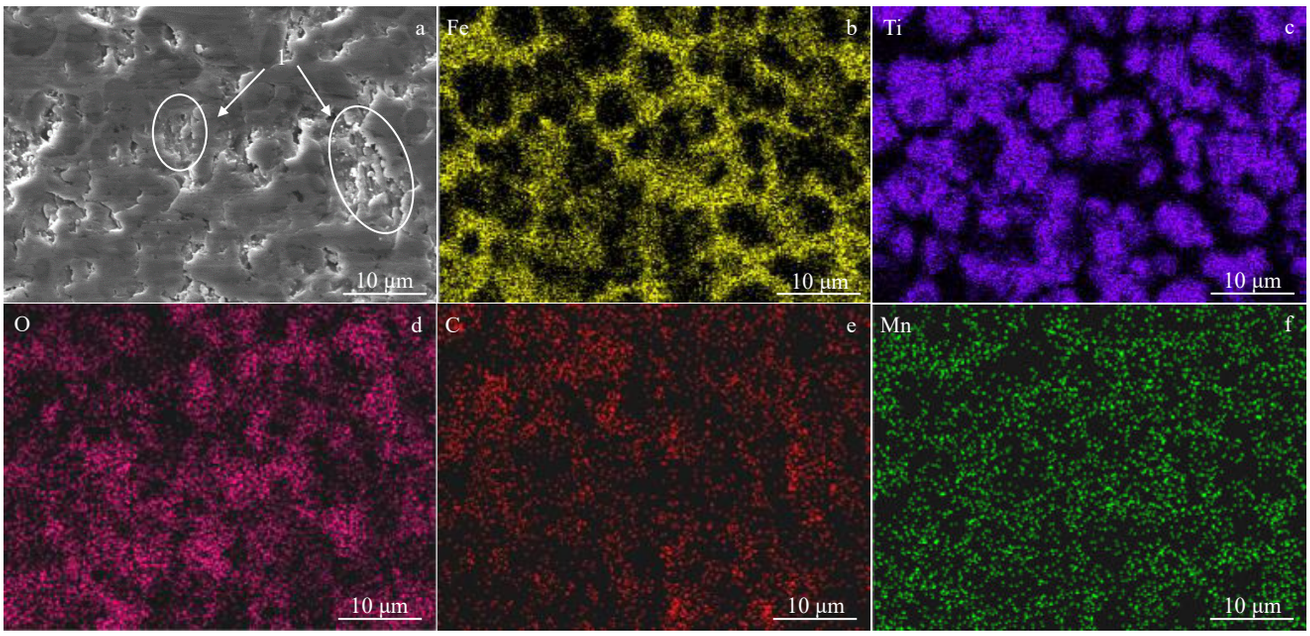

Fig.15 SEM morphology (a) and EDS mappings (b–f) of friction wear of laser cladding coating

3 Conclusions

1) Powder reinforcement of dispersed TiC micron ceramic particles creates a self-gradient coating. The coating and powder phases are composed of the austenite phase, the ceramic phase, and trace ferrite. There is a good metallurgical bonding between the coating and the substrate. The Vickers hardness of the coating increases the gradient from the bottom to the top.

2) The TiC ceramic phase in the lower part of the coating exhibits three different growth modes: dendritic, dispersed, and partially agglomerated into a "satellite ball" shape. The number of TiC ceramic phases gradually increases in the middle, and the TiC particles in the upper part are denser than those in the lower and middle parts and grow in a bridging growth mode. The ceramic phase is affected by surface tension and buoyancy, and the number of ceramic particles increases the gradient from the bottom to the top, so the Vickers hardness increases the gradient.

3) The TiC-reinforced particles used to form the cladding layer have superior friction and wear characteristics. When evaluated from the two-dimensional profile, it can be seen that the wear depth of the substrate is five times larger than that of the coating, and the cladding coating significantly improves the wear resistance of the coated 40Cr components.

References

1 Chen Huahui, Xing Jiandong, Li Wei. *Application Manual of Wear Resistant Materials*[M]. Beijing: Mechanical Industry Press, 2006: 121 (in Chinese)

2 Zhou K. *Additive Manufacturing: Materials, Functionalities and Applications*[M]. Cham: Springer Nature, 2022

3 Chiulan I, Voicu S I, Batalu D. *Applied Sciences*[J], 2022, 12(7): 3521

4 Friend C M, Horsfall I, Burrows C L. *Journal of Materials Science*[J], 1991, 26: 225

5 Zhu C, Zhang B, Zheng S. *Materialwissenschaft und Werkstofftechnik*[J], 2020, 51(2): 247

6 Glaeser W. *Materials for Tribology*[M]. Amsterdam: Elsevier, 1992

7 Bendikiene R, Ciuplys A, Kavaliauskiene L. *Journal of Cleaner Production*[J], 2019, 229: 1225

8 Liu Y, Ding Y, Yang L *et al. Journal of Manufacturing Processes*[J], 2021, 66: 341

9 Zhu L, Xue P, Lan Q *et al. Optics & Laser Technology*[J], 2021, 138: 106915

10 Jiang S, Huang L, Gao X *et al. Acta Materialia*[J], 2021, 203: 116456

11 Zhang S. *Materials Science and Engineering A*[J], 1993, 163(1): 141

12 Ma Baoxia, Xu Yang, Xu Dunhao *et al*. *Rare Metal Materials and Engineering*[J], 2023, 52(8): 2791 (in Chinese)

13 Cai Y, Zhu L, Cui Y *et al. Applied Surface Science*[J], 2021, 543: 148794

14 Wu Hao, Zhang Long, Yu Jiashi *et al*. *Rare Metal Materials and Engineering*[J], 2023, 52(6): 2205 (in Chinese)

15 Mao H, Shen F, Zhang Y *et al. Coatings*[J], 2021, 11(12): 1444

16 Wang Jian, Zhang Pingxiang, Hu Rui *et al. Rare Metal Materials and Engineering*[J], 2015, 44(5): 1169 (in Chinese)

17 Li C. *Journal of Physics: Conference Series*[C]. Guizhou: IOP Publishing, 2023, 2419(1): 012049

18 Li Jiawen, Liu Sicong, Huang Sirui *et al*. *Rare Metal Materials and Engineering*[J], 2023, 52(4): 1169

19 Yang S, Zhong M, Liu W. *Materials Science and Engineering*

A[J], 2003, 343(1–2): 57
20 Xu X, Mi G, Xiong L *et al. Journal of Alloys and Compounds*[J], 2018, 740: 16
21 Liu Y H, Li J, Xuan F Z. *Surface Engineering*[J], 2012, 28(8): 560
22 Zhang Y, Wei Z, Shi L *et al. Journal of Materials Processing Technology*[J], 2008, 206(1–3): 438
23 Gu D, Hagedorn Y C, Meiners W *et al. Composites Science and Technology*[J], 2011, 71(13): 1612
24 Qi K, Yang Y, Sun R *et al. Materials Letters*[J], 2021, 282: 128893
25 Zhao Mingjuan, Hu Yong, Fu Shengqi *et al*. *Rare Metal Materials and Engineering*[J], 2022, 51(12): 4632 (in Chinese)
26 Lu C, Zhang R, Wei X *et al. Applied Surface Science*[J], 2022, 586: 152796
27 Lee C S, Oh J C, Lee S. *Metallurgical and Materials Transactions*[J], 2003, 34(7): 1461
28 Ning Jiapei, Zheng Kaihong, Wang Juan *et al. Rare Metal Materials and Engineering*[J], 2020, 49(7): 2407 (in Chinese)
29 Shi Chenxiao, Liu Yuanfu, Zhang Lele *et al*. *Rare Metal Materials and Engineering*[J], 2021, 50(8): 2686
30 He X, Song R G, Kong D J. *Optics & Laser Technology*[J], 2019, 112: 339
31 Paulo J. *Tribology for Engineers*[M]. Comwall: Woodhead Publishing, 2011
32 Kragelsky I V, Dobychin M N, Kombalov V S. *Friction and Wear: Calculation Methods*[M]. London: Elsevier, 2013
33 Smolin A, Shilko E, Grigoriev A *et al. Continuum Mechanics and Thermodynamics*[J], 2022, 35(4): 1353
34 Gleason G, Bailey K, Sunny S *et al. Journal of Manufacturing Processes*[J], 2022, 80: 480
35 Yoshizawa H, Chen Y L, Israelachvili J. *The Journal of Physical Chemistry*[J], 1993, 97(16): 4128
36 Arnell D. *Mechanisms and Laws of Friction and Wear// Tribology and Dynamics of Engine and Powertrain*[M]. Cornwall: Woodhead Publishing, 2010: 41
37 Hurricks P L. *Wear*[J], 1973, 26(3): 285
38 Li B, Zhang S, Wang R *et al. Journal of Materials Research and Technology*[J], 2019, 8(5): 3811
39 Chen Lulu, Zhai Hongxiang, Huang Zhenying *et al. Rare Metal Materials and Engineering*[J], 2018, 47(S1): 407 (in Chinese)
40 Hu Wenqiang, Huang Zhenying, Zhai Hongxiang *et al. Rare Metal Materials and Engineering*[J], 2018, 47(S1): 155 (in Chinese)
41 Jiang Jipeng, Li Shibo, Hu Shujun *et al. Rare Metal Materials and Engineering*[J], 2020, 49(2): 701 (in Chinese)

激光熔覆 TiC 颗粒增强 Fe 基梯度涂层的耐磨性能

刘鹏宇[1]，李　辉[1,3]，张瑞华[1,2]，肖梦智[1]，魏小红[2]，尹　燕[2,4]，屈岳波[1]，路　超[2,5]

(1. 钢铁研究总院，中国 北京 100081)

(2. 阳江市五金刀剪产业技术研究院，广东 阳江 529533)

(3. 四川轻化工大学 过程装备与控制工程四川省高校重点实验室，四川 自贡 643000)

(4. 兰州理工大学 材料科学与工程学院，甘肃 兰州 730050)

(5. 广东海洋大学 材料科学与工程学院，广东 阳江 529500)

摘　要：采用激光熔覆的方法将TiC颗粒增强铁基粉末熔覆在40Cr钢基体上制备高硬度耐磨梯度陶瓷涂层。利用扫描电镜（SEM）、能谱仪（EDS）、X射线衍射仪（XRD）、显微硬度计、摩擦磨损试验机对熔覆层的微观组织、物相、硬度及耐磨性进行研究。结果表明：熔覆层物相主要为奥氏体相、TiC强化相，并有少量铁素体相，激光熔覆TiC颗粒增强粉末制备的金属陶瓷涂层组织致密、物相与粉末组成基本一致；TiC强化相在熔池底部到顶部呈梯度分布，熔池中TiC强化相部分溶解、尺寸减小，部分受激光热作用长大呈四方形、雪花状、鱼骨状，TiC相在熔池底部呈现3种生长方式，且TiC增强相分布较少，熔池中部TiC增强相逐渐增多，熔池上部TiC增强相出现富集并桥接生长；熔覆层维氏硬度HV高达19 602.94 MPa，同等条件下，涂层的摩擦磨损深度为基体的1/5，显著提高了基体的耐磨性。

关键词：激光熔覆；TiC；金属陶瓷；组织性能

作者简介：刘鹏宇，男，1991年生，博士，工程师，钢铁研究总院，北京 100081，电话：0662-3837260，E-mail：lpyhj@foxmail.com